Available online at www.sciencedirect.com
SCIENCE DIRECT®
International Journal of Heat and Fluid Flow 26 (2005) 276–288
International Journal of HEAT AND FLUID FLOW
www.elsevier.com/locate/ijhff

Reduced-order description of fluid flow with moving boundaries by proper orthogonal decomposition

Yogen Utturkar, Baoning Zhang, Wei Shyy *

Department of Mechanical and Aerospace Engineering, University of Florida, Gainesville, FL 32611, USA

Accepted 26 August 2004
Available online 19 October 2004

Abstract

The approach of proper orthogonal decomposition (POD) has been extensively adopted for fluid dynamics in fixed geometries. This technique is examined here for fluid flow with moving boundaries; in the context of cavitating and phase change flows, and fluid–membrane interaction. The purpose is to assess the capability of POD in extracting the salient features and offering a compact representation to the CFD solutions associated with boundary movement. The cavitating flow simulations are investigated to distill the effect of turbulence modeling, between the Launder–Spalding and a filter-based turbulence models. The lower-order eigenmodes of the flow field, for both turbulence models, show different flow structures and global parameters between higher and lower cavitation numbers. The effect of multi-timescales produced by the filter-based turbulence model is discerned by POD analysis. For 3-D, membrane wing flows, very few POD modes seem sufficient for accurate representation of the velocity field. However, reduced-order analysis of the aerodynamic performance, which is strongly dictated by pressure, may be coarsened by moving membrane dynamics. The flow with fusion is further considered for its solid–liquid phase front propagation. While few modes can sufficiently construct the flow field for the later interval of the flow, a larger number of POD modes are required to provide the flow scales for the initial part of the phase change process.

Keywords: Proper orthogonal decomposition; Moving boundaries; Phase change

1. Introduction

The art of scientific computations has lately received impetus due to the improvement in computer hardware resources. With the advent of faster processors, efficient memory modules, and parallel computing techniques, simulation of complex phenomena in nature is becoming increasingly feasible. However, the challenges in performing a computation and analyzing the available data, increase manifold with the level of complexity in the governing equations. Despite the fact, efforts in encountering these difficulties are rewarding. Numerical simulations yield comprehensive data, which may be impractical as an experimental task. These data not only provide deep insight into the physics of the problem, but also concurrently assist in the appraisal and enhancement of various models that are deployed for the computations.

Effective utilization of the colossal information yielded by simulations certainly merits development of efficient post-processing strategies. Any tool that offers a succinct expression to the available data is obviously a great asset to the computational endeavor. In the present study, we focus on the capabilities of the statistical technique of proper orthogonal decomposition (POD), in context of probing flows with moving boundaries. POD essentially captures intrinsic and salient flow structures of a time-dependent field by a statistical approach.

* Corresponding author. Tel.: +1 352 392 0961; fax: +1 352 392 7303.
E-mail address: wss@mae.ufl.edu (W. Shyy).

0142-727X/$ - see front matter © 2004 Elsevier Inc. All rights reserved.
doi:10.1016/j.ijheatfluidflow.2004.08.008

Nomenclature

q	flow variable/quantity
r	spatial location
t	time
u, v, w	velocity components
p	pressure
T	temperature
k	turbulent KE
ε	turbulent dissipation
ρ	density
μ	viscosity
c	speed of sound
γ	ratio of specific heats
U	velocity scale
Δ	filter size
$\Im$	filter function
F	objective error function
ψ	basis function
ϕ	scalar coefficient
λ	eigen value
s	singular value
R	cross-correlation tensor
E	energy content
A, U, Σ, V, Γ, E	matrices
Ω	domain
N	total DOF = number of time steps
k, M, n	row/column indices
C_1, C_2	constants
St, Ra and Pr	Stefan, Rayleigh and Prandtl number respectively
σ	cavitation number

Subscripts/Superscripts

m	mixture
l	liquid
v	vapor
∞	far field
0	at boundaries
t	turbulent
$'$	fluctuation

It yields a set of orthogonal basis functions, termed as 'POD modes' or 'eigenmodes', which capture the principle flow features. The extraction of eigenmodes is further complimented by a rapid convergence of the energy associated with each mode. Consequently, a reduced-order investigation of the data is facilitated through a fewer number of POD modes.

POD was first introduced by Lumley (1967) to investigate coherency of turbulent flow structures. Since this seminal contribution, POD has been a popular tool to extract systematically hidden, but deterministic, structures in turbulent flows and can be extensively found in literature. Gradual progress in this area has established the application of this technique to laminar flows, as well as to flows under incompressible and compressible conditions. The latest studies and relevant issues of POD implementation are reviewed hereafter. Aubry et al. (1988) built a five-mode, reduced-order model for the wall region of a fully turbulent channel. Their effort was extended by Podvin (2001), who provided numerical validation of a ten-dimensional model for the wall layer. The ability of the ten-dimensional model to produce intermittent features, which are reminiscent of bursting process in a wall layer, was also demonstrated. Comprehensive POD studies on turbulent mixing layers are available (Delville et al., 1999; Ukeiley et al., 2001), which not only identify the large-scaled structures in the layer, but also model the dynamic behavior of the lower-order modes. Prabhu et al. (2001) explored the effect of various flow control mechanisms in a turbulent channel, on the flow structure in POD modes. The POD modes of various flow control mechanisms showed significant differences close to the wall but were similar in the channel core. Similarly, while Liberzon et al. (2001) employed POD to study vorticity characterization in a turbulent boundary layer, Kostas et al. (2002) adopted the approach to probe PIV data for the backward-facing step flow. Picard and Delville (2000) investigated the effect of longitudinal pressure distribution on velocity fluctuations in the turbulent shear layer of a subsonic round jet, using POD. Annaswamy et al. (2002) examined 'edge-tones' of an aircraft nozzle by analyzing the POD modes of azimuthal pressure distribution of a circular jet. Cizmas and Palacios (2003) gained insight on the turbine rotor–stator interaction with a lower-order POD investigation. They effectively utilized the time history and phase-plane plots of the POD coefficients to unravel the key dynamics in the flow behavior. POD-based investigations on pulsed jet flow field (Bera et al., 2001), temperature field in flow over heated waves (Gunther and Rohr, 2002), and many such flow cases provide further evidence on the wide applicability of the technique. As mentioned earlier, POD has been successfully extended to laminar flow cases for extracting the principle features from time-dependent flow data (Ahlman et al., 2002).

Despite the ongoing progress in POD, several issues of its applicability to variable density and compressible flow are lately being examined. As indicated before, POD essentially yields a series, which rapidly converges towards the norm of a variable $q(r,t)$. Several

past studies intuitively adopted scalar-valued norms for the convergence criterion. For example, each flow variable namely pressure, density, or any velocity component was separately decomposed into POD modes. However, Lumley and Poje (1997) observed that for variable density flows, such as buoyancy-driven flows, an independent POD analysis may decouple the physical relationship between the flow variables. They suggested that the norm selection should incorporate the density variations into the velocity field, to achieve the convergence of a physically relevant quantity—mass rather than mere velocities—through the POD procedure. However, simultaneous use of two flow variables also poses an important issue of deciding the significance of each variable in convergence process. Lumley and Poje (1997) suggested a vector form to $q(r,t)$ as $q(r,t) = [C_1u, C_1v, C_1w, C_2\rho']$. In addition, they provided a mathematical analysis to optimize the values of the weighing factors for expediting the convergence. Colonius et al. (2002) extended the above argument by examining the impact of the norm selection on POD analysis of compressible flow over a cavity. POD modes independently obtained by scalar-valued norms of pressure and velocity were compared to those derived by vector-based norms. The choice of the vector, $q(r,t) = [u, v, w, \sqrt{\frac{2}{\gamma-1}}c]$, was chosen with ingenuity so as to yield a norm as shown below:

$$\|q(r,t)\| = \left[\int_\Omega \left(u^2 + v^2 + w^2 + \frac{2}{\gamma-1}c^2\right) \mathrm{d}r^3\right]^{\frac{1}{2}} \tag{1}$$

The above norm effectively yielded a linear series that converged towards the stagnation enthalpy instead of mere kinetic energy. Colonius et al. (2002) further reported that scalar-valued POD modes were unable to capture key processes such as acoustic radiation, which heavily rely on coupling mechanisms between the variables. In comparison, the vector-valued POD modes were in cohort with the compressible flow dynamics. Ukeiley et al. (2002) employed $q(r,t) = [\frac{\rho}{\rho_\infty}, \frac{u}{U_\infty}, \frac{v}{U_\infty}, \frac{w}{U_\infty}, \frac{T-T_\infty}{T_0-T_\infty}]$ to perform POD on numerical data of compressible mixing layer. The variables, as shown above, were normalized by their freestream values to ensure a rational weighing of their fluctuations. A slow convergence towards the multi-variable norm was reported. POD implementation was also shown to face serious issues in case of supersonic flows due to presence of shock fronts. Lucia et al. (2002) noticed that though the bulk flow can be modeled by few eigenmodes, a larger number of eigenmodes are required to accurately capture the discontinuity in the flow. They circumvented the issue by employing domain decomposition in their POD implementation. Though reasonable success in the reduced-order representation of the shock was reported, issues of extending the decomposition technique to moving shock fronts are still unresolved.

In this study, we extend the POD methodology to investigate three distinct cases of time-dependent simulations. While two of the chosen cases are two-phase flow problems, the third case comprises fluid–structural interaction. To the best of our knowledge, the efficacy of POD representation in context of either two-phase flows or aeroelasticity problems has been insufficiently probed. The existence of a moving boundary, and in turn its numerical modeling strategy register a significant impact on the dynamic behavior of the solution and the flow scales. As a result, there is a need to assess the fidelity of POD representation for such computations to instill confidence into the approach. Furthermore, some of the computations investigated in this study are fairly exploratory, with the use of newly developed models and insufficient experimental support. The eigenmodes and the unsteady behavior of their respective scalar coefficients for these computations are employed to distill the impact of the numerical models on the solution. Thus, a twofold objective of *appraisal* and *examination* of *reduced-order flow description* for three distinct and interesting simulations motivates the present endeavor.

2. Mathematical background

Consider a flow quantity, $q(r,t)$, where r denotes spatial variables and t denotes time. The objective of POD can be simply stated as minimizing the L_2 norm of the objective error function, $F_k(r,t)$, which is defined as (Lumley, 1967; Delville et al., 1999; Ukeiley et al., 2001; Ahlman et al., 2002; Arian et al., 2002):

$$F_k(r,t) = q(r,t) - q^k(r,t) \tag{2}$$

The L_2 norm in terms of volume integral can be defined as:

$$\|F_k(r,t)\| = \left[\int_\Omega F_k^2(r,t)\,\mathrm{d}r^3\right]^{\frac{1}{2}} \tag{3}$$

Here, $q^k(r,t)$ denotes the data projected with a linear combination of certain number (k) of orthogonal basis functions ($\psi(r)$). Through calculus of variations, the problem of determining the optimally converging basis modes, $\psi(r)$, can be well-posed in form of an integral equation as shown (Lumley, 1967; Delville et al., 1999):

$$\int_\Omega R(r,r')\psi(r')\,\mathrm{d}r' = \lambda\psi(r) \tag{4}$$

where, $R(r,r')$ is the space correlation tensor, defined as:

$$R(r,r') = \langle q(r,t)q(r',t)\rangle \tag{5}$$

In the context of classical application of POD to turbulent structures, the angular brackets denote ensemble average of statistically stationary turbulent flow data. However, the angular brackets in context of the present

study interchangeably represent time-averaging of either unsteady RANS or laminar solutions. This approach is often referred in literature as the 'snapshot POD approach' (Sirovich, 1987; Zhang et al., 2003), where every instantaneous solution is considered as a 'snapshot' of the data. Solution of Eq. (4), which is also subjected to a constraint of unitary norm $|\psi(r)| = 1$, yields the orthogonal eigenmodes $\psi_n(r)$ with corresponding eigenvalues λ_n. Consequently, solution of the flow quantity at each time step can be exactly expressed as a linear combination of the eigenmodes (also known as POD modes) in the following form.

$$q(r,t) = \sum_{n=1}^{N} \phi_n(t)\psi_n(r) \tag{6}$$

The time-dependent multipliers or scalar coefficients, $\phi_n(t)$, are obtained by projecting the solution at each time step on the basis functions as shown.

$$\phi_n(t) = \int_{\Omega} q(r,t)\psi_n(r)\,\mathrm{d}^3 r \tag{7}$$

Merely, from a standpoint of Eq. (6), infinite choices for the basis functions $\psi_n(r)$ are available. But, the basis functions determined in conjunction with the minima of $|F_k(r,t)|$ensure optimal and sequential extraction of key features from the data ensemble, enabling truncation of the series (6) with fewer POD modes. Thus, succinct expression of a voluminous data ensemble, with focus on its salient aspects is facilitated through the lower-order modes.

3. Numerical procedure

In the current study, the CFD solution at every time step is considered as a snapshot of the flow field, and an ensemble in form of a matrix A is generated as follows:

$$A = [a_1, a_2, a_3, \ldots, a_N] \tag{8}$$

where, $a_n \in R^M$; $n = 1,2,3,\ldots,N$ denotes the solution at all M nodes in the domain at the nth time step (usually $M \gg N$). Thus, when $q(r,t)$ is expressed in the above matrix form, the solution of Eq. (4) reduces to obtaining the eigenvalues and eigenvectors of the matrix AA^{T}, which is achieved by the numerical technique of singular value decomposition (SVD).

3.1. Singular value decomposition (SVD)

Any real matrix $A_{M\times N}$ can be decomposed into the form (Zhang et al., 2003):

$$A = U\Sigma V^{\mathrm{T}} \tag{9}$$

where, U is a $(M \times M)$ matrix whose columns form left singular vectors; V is a $(N \times N)$ matrix whose columns form right singular vectors, and Σ is a pseudo-diagonal $(M \times N)$ matrix whose diagonal elements are the singular values s_n. Furthermore, it can be easily shown that the eigenvalue decomposition of the matrix AA^{T} can be expressed as:

$$AA^{\mathrm{T}} = U\Sigma^2 U^{\mathrm{T}} \tag{10}$$

From Eqs. (9) and (10), it is evident that eigenvalues of AA^{T} are squares of the singular values of A ($\lambda_n = s_n^2$), and its eigenvectors are the left singular vectors of A. Thus, SVD of the ensemble matrix A can effectively yield the desired POD basis functions and their respective eigenvalues. The SVD in present study is performed with the subroutine—Householder reduction to bi-diagonal form and diagonalization by QR procedure with shifts (Press et al., 1992).

3.2. Post-processing the SVD output

The SVD subroutine returns the matrix U with $M \times M$ elements. The matrix U is reshaped by extracting only its first N columns. The resultant matrix U, which is now an $M \times N$ matrix, comprises the N eigenmodes corresponding to the original data in matrix A. Note that the constraint $|\psi(r)| = 1$ manifests itself in the following form

$$U^{\mathrm{T}}U = I \tag{11}$$

where, I is an $N \times N$ identity matrix. The coefficient matrix for $\phi_n(t)$, in compliance with Eq. (7), is further obtained as:

$$\Gamma = U^{\mathrm{T}}A \tag{12}$$

Subsequently, the truncated series with k eigenmodes, in form of another matrix, $\widehat{A}(k)$, is constructed as follows:

$$\widehat{A}(k) = \widehat{U}_{M\times k}\widehat{\Gamma}_{k\times N} \tag{13}$$

where, $\widehat{U} \in U$ and $\widehat{\Gamma} \in \Gamma$. It is thus straightforward to observe that the error/discrepancy between the actual and reconstructed data is

$$\mathrm{E}(k) = A - \widehat{A}(k) \tag{14}$$

The fraction of cumulative energy captured by k eigenmodes is calculated as follows (Ahlman et al., 2002; Zhang et al., 2003):

$$E_k = \frac{\sum_{n=1}^{k}\lambda_n}{\sum_{n=1}^{N}\lambda_n} = \frac{\sum_{n=1}^{k}s_n^2}{\sum_{n=1}^{N}s_n^2} \tag{15}$$

The energy fractions and the error matrix (Eq. (14)) are commonly used parameters to judge a POD representation.

4. Results and discussion

We discuss the results of POD analysis on three flow cases having distinct characteristics. Only the relevant points of the numerical approach are briefly delineated

for each case. For elaborate discussion on the respective methodologies, the reader is referred to the original studies (Wu et al., 2003b; Senocak and Shyy, 2002; Senocak and Shyy, 2004a,b; Zhang et al., 2003; Lian et al., 2003; Utturkar et al., 2004). For all the cases discussed, we perform POD without subtracting the time-averaged value from the data. As a consequence, the first eigenmode is likely to resemble the time-averaged solution. However, this approach enables us to examine the eigenmodes with a consistent perspective. Furthermore, two of the cases discussed below represent incompressible flows, while the variable density effects in the cavitating flow cases are localized to a relatively small region in the entire domain. We thus implement SVD separately for each variable for simplicity.

4.1. Turbulent cavitating flow around a hydrofoil

Numerical modeling of turbulent cavitating flow is currently an area of active research with several unresolved issues and challenges. The main causes of these challenges are the complex dynamics of the liquid–vapor interface and the multi-timescales in the flow. We choose to probe the available data of 2-D, RANS-based turbulent cavitating flow computations for a hydrofoil geometry (Wu et al., 2003b), by employing POD. Totally 250 time steps are collected for the POD analysis. The cavitating flow computations are based on the single-fluid modeling approach. Thus, the variable density field is represented by a liquid-phase fraction, which is obtained by solving its transport equation (Senocak and Shyy, 2002). The present hydrofoil simulations are computed on a stationary, curvilinear grid comprising multiple blocks, by a pressure-based solver (Thakur et al., 2002). Due to infeasibility of LES or direct simulation approach for multiphase flows, the two-equation based k–ε modeling strategy is adopted, with two different formulations for predicting the eddy-viscosity. The first formulation is the commonly employed Launder and Spalding model (1974), where the eddy viscosity is formulated as:

$$\mu_t = \frac{0.09\rho_m k^2}{\varepsilon} \tag{16}$$

The second formulation, which is the filter-based model, is as shown below (Johansen et al., 2004).

$$\mu_t = \frac{0.09\rho_m k^2}{\varepsilon}\Im$$
$$\Im = \mathrm{MIN}\left(1, \frac{\Delta\varepsilon}{k^{3/2}}\right) \tag{17}$$

Here, the filter-function $\Im$ conditionally controls the dissipation based on the chosen filter size (Δ). If the size of Δ, which is a control parameter in the simulation, can adequately address the turbulent length scale ($\Delta \ll \frac{k^{3/2}}{\varepsilon}$), then the flow is computed directly. Conversely, a coarse filter size recovers $\Im = 1$, and subsequently implements the Launder and Spalding model (1974). A value of $\Im = 1$ is also imposed on 'no-slip' boundaries to enable the use of wall functions. Recent computations (Wu et al., 2003a) demonstrated that certain phenomena such as periodic detachment and shedding of the vapor cavity, which arise from cavitation instabilities, are excessively damped by the Launder and Spalding model (1974). The filter-based model, which significantly improved the prediction in case of single-phase flow past a cylinder (Johansen et al., 2004), is thus adopted as a remedy in case of the hydrofoil calculations. This is the first implementation of the filter-based model on a multiphase computation. Moreover, the hydrofoil computations are in compliance to a common, conference test case with lack of experimental data to date. The following discussion serves to probe the effect of the two models on the computation, within the available resources, to gain insight for further improvement.

Fig. 1 illustrates a sample snapshot of the solution along with the lift/drag behavior of the hydrofoil. The cavitation number, which is defined as $\sigma = \frac{p_\infty - p_v}{0.5\rho_l U_\infty^2}$, is inversely related to the cavitation (void formation) intensity. The two turbulence models induce a drastic difference into the solution, as seen from the aerodynamic coefficients. Firstly, they produce a significantly different mean value of lift coefficient at both the cavitation numbers. Secondly, at both the σ values, the Launder and Spalding model decays to attain a quasi-steady state, while the filter-based model sustains the oscillations. Furthermore, the unsteadiness at the higher cavitation is largely characterized by a single frequency. Conversely, the filter-based model, in particular, illustrates a multi-timescale pattern at $\sigma = 0.4$. The nature and the order of impact of these observations on the flow structure can be assessed from the streamline plots in Fig. 2, while the dynamic pattern of this structure can be further observed from the scalar coefficients depicted in Figs. 3 and 4. Note that the velocity field comprises a mean flow component and the fluctuations caused by flow instabilities. Thus, the first eigenmode (Fig. 2) identifies itself greatly with the mean flow behavior, while the later eigenmodes agglomerate the variance. The turbulence models do not noticeably influence the mean flow structure, which constitutes at least 99% of the flow energy in either case. At $\sigma = 0.8$, even the second and third POD modes appear consistent, pointing that the two turbulence models do not impact the lower-order flow structures. The dynamic behavior at the higher cavitation number, observed in Fig. 1(b), is appreciably manifested into the first scalar coefficient, as seen in Fig. 3. Conversely, the flow field at the lower cavitation number is much more sensitive to the turbulence closure. Though the first POD mode is consistent (Fig.

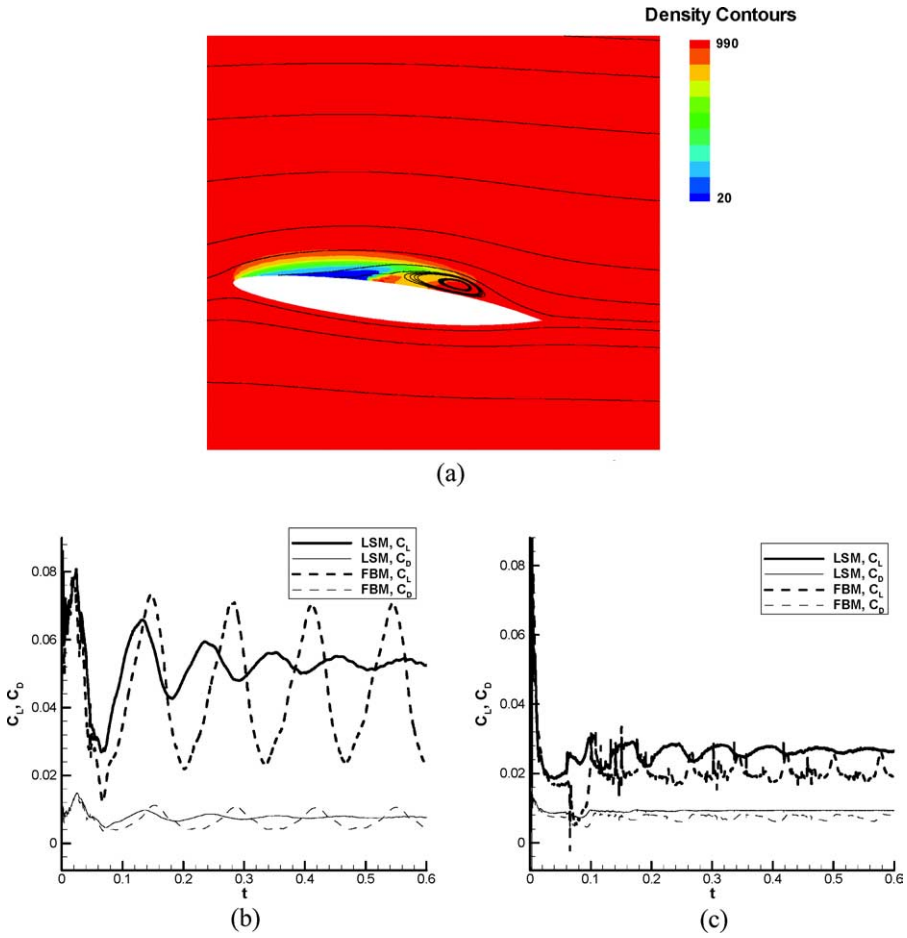

Fig. 1. Results of cavitating flow from CFD computations; LSM: Launder and Spalding model; FBM: filter-based model (Wu et al., 2003b). (a) Instantaneous solution (density contours, kg/m^3 and streamlines); $\sigma = 0.4$. (b) Lift and drag; $\sigma = 0.8$. (c) Lift and drag; $\sigma = 0.4$.

2), the two models clearly impact the flow structures in the second and third eigenmode indicating a second-order effect. This observation can be attributed to the multi-timescale behavior shown by the filter-based model (Fig. 1(c)), which is not adequately represented within the dynamics of the first mode (Fig. 3), unlike the earlier case. As a consequence, the effect pervades into the succeeding modes by inducing dissimilar flow patterns. The phase plots of the scalar coefficients, which are shown in Fig. 4, couple the lower-order POD modes via a dynamic framework. The scalar coefficients of the lower-order modes, as seen from the plots, are dominated by a well-ordered harmonic behavior. The limit cycle phenomenon in the filter-based model coefficients underscores the sustenance of cavitation instabilities. The alternate model, however, dissipates these instabilities at all the significant energy levels. Thus, the phase plane plots clearly endorse the ability of the filter-based model to modulate the eddy viscosity.

The efficacy of the POD representation in the hydrofoil case can be appraised from Fig. 5. As discussed before, the lift coefficient, especially with the filter-based modeling approach, demonstrates pronounced unsteady behavior, which in turn points to the wide ranging oscillations in the hydrofoil surface pressure. The recovery of the dynamic pattern in these oscillations is thus sufficient to justify the reduced-order examination. Fig. 5 illustrates that first five eigenmodes reasonably retrieve the unsteady features of the hydrofoil surface pressure, at the lower cavitation number. The pressure coefficient, as depicted in Fig. 5, is defined as $C_p = \frac{p-p_\infty}{0.5\rho_l U_\infty^2}$. Because of the heavy dependence of lift and drag on surface pressure, the above observation is encouraging for constructing lower-order, hydrodynamic flow models.

4.2. Laminar flow around a 3-D membrane wing

The laminar flow computations around a 3-D membrane wing discussed in this section are mainly motivated by the increasing research interest in micro-aerial vehicles (MAV) (Lian et al., 2003). The membrane wing, which is modeled with a zero thickness, imposes a moving boundary inside the computational domain. The shape of the membrane changes dynamically in response to the fluid stresses. In fact, the frequency of wing vibration differs from the overall fluid timescale by an $O(100)$

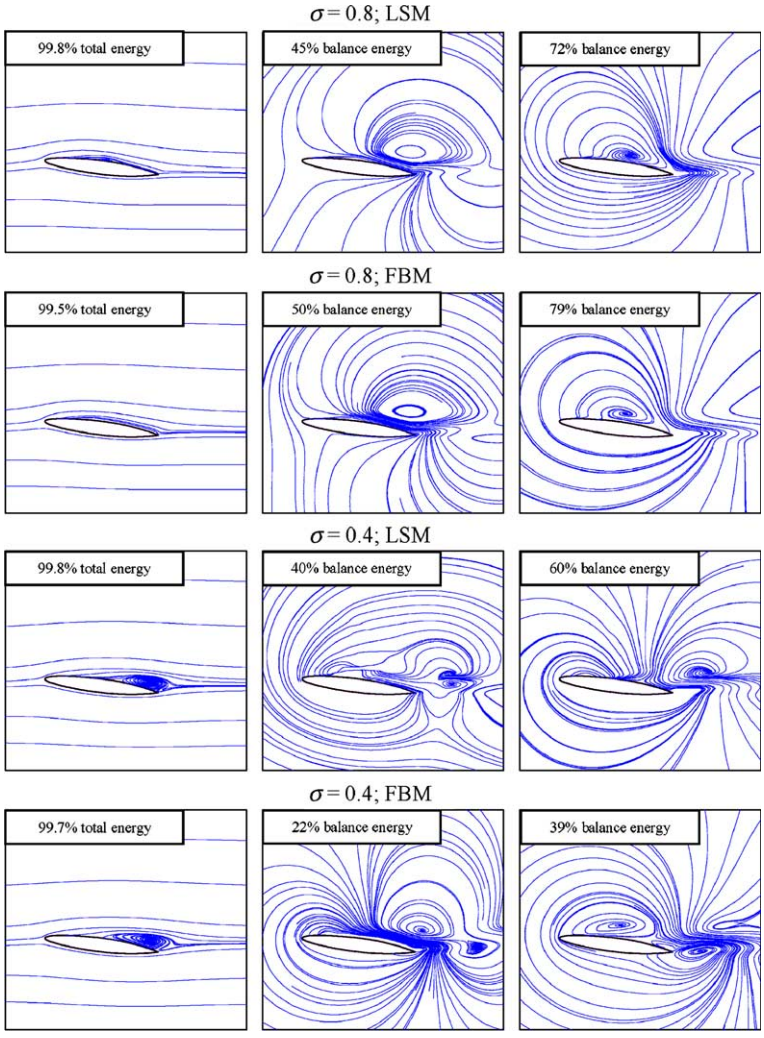

Fig. 2. POD modes showing velocity streamlines; $\psi_i(r)$; $i = 1,2,3$; $q(r,t) = \vec{V}(r,t)$; LSM: Launder and Spalding model; FBM: filter-based model.

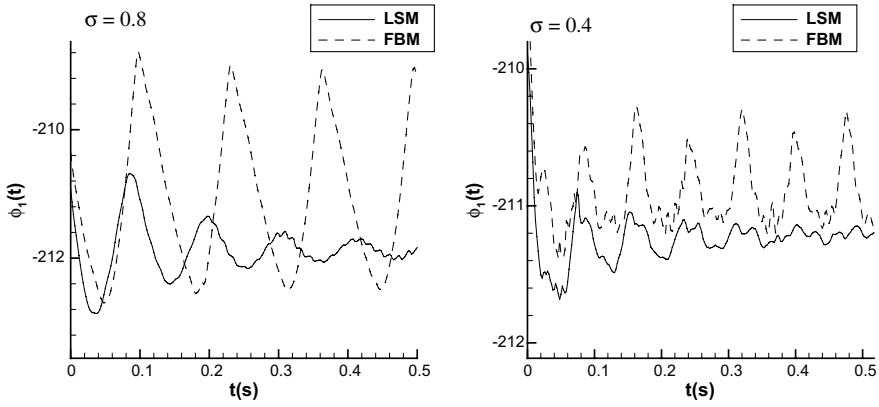

Fig. 3. Time-dependent behavior of first scalar coefficient ($\phi_1(t)$); $q(r,t) = \vec{V}(r,t)$; LSM: Launder and Spalding model; FBM: filter-based model.

factor. This membrane vibration superimposes pronounced unsteady effects over the steady mean flow. The CFD computation of such problems with fluid–structural interaction is usually expensive and generates huge amount of data. We employ POD to probe the available data efficiently. The impact of moving membrane on the flow structure is distilled by contrasting the results to a computation under rigid wing condition. All the simulations are computed on a body-fitted grid with second-order upwind scheme for convection and

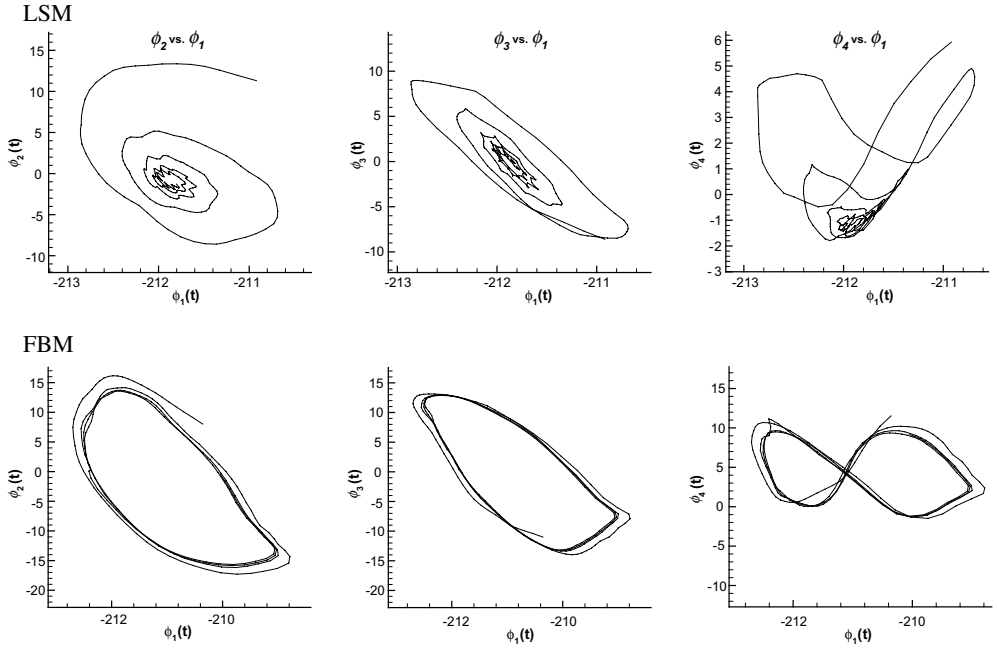

Fig. 4. Phase plane plots of scalar coefficients for $\sigma = 0.8$; $q(r,t) = \vec{V}(r,t)$; LSM: Launder and Spalding model; FBM: filter-based model.

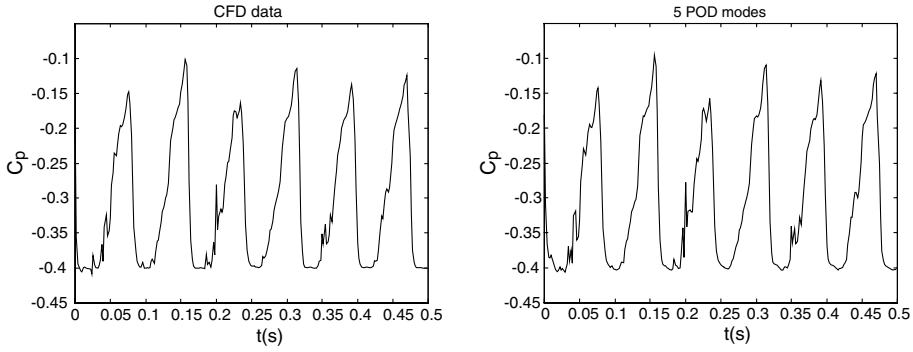

Fig. 5. Time history of pressure coefficient on the hydrofoil surface at 90% chord length; $\sigma = 0.4$; filter-based model; $q(r,t) = p(r,t)$.

central differencing for pressure and viscous terms (Lian et al., 2003; Zhang et al., 2003). The computational domain of the wing geometry and a snapshot of the solution are depicted in Fig. 6.

Overall, 95 time steps, which comprise three periods of the convective flow time-scale, are used in the POD implementation. The Reynolds number, based on the free stream velocity and the chord length, is 9×10^4. Since lift and drag characteristics are of main interest, POD is performed on a smaller region around the membrane wing. The issue of the time-variant grid is circumvented by interpolating the solution at each time step on to a fixed uniform grid, by an inverse-distance interpolation method (Zhang et al., 2003). Two membrane wing cases with angle-of-attack (hereafter AOA) equal to 6° and 27° are compared to a rigid wing case with AOA equal to 6°.

The eigenmodes of the velocity field for the three cases are illustrated in the streamline plots of Fig. 7. The first mode, which is consistent with the mean flow properties, captures at least 99% of the kinetic energy in all three cases. Nonetheless, the moving membrane in particular indicates a larger fluctuating component, which in turn increases with the AOA. The membrane wing, when compared to the rigid wing, negligibly affects the flow structure in first eigenmode, while the second eigenmode is moderately impacted. However, the differences in the higher-order flow structures are much more conspicuous, as indicated by the third POD mode. Comparatively, the effect of AOA is strongly registered even on the first POD mode, as seen from Fig. 7.

Investigations in the area of MAV mainly focus on the lift and drag performance of the wing. In the present case, calculation of viscous drag from the fixed grid is a non-trivial task. Furthermore, the form drag accounts for a large portion of the total drag force. We thus neglect the viscous forces and account only the pressure

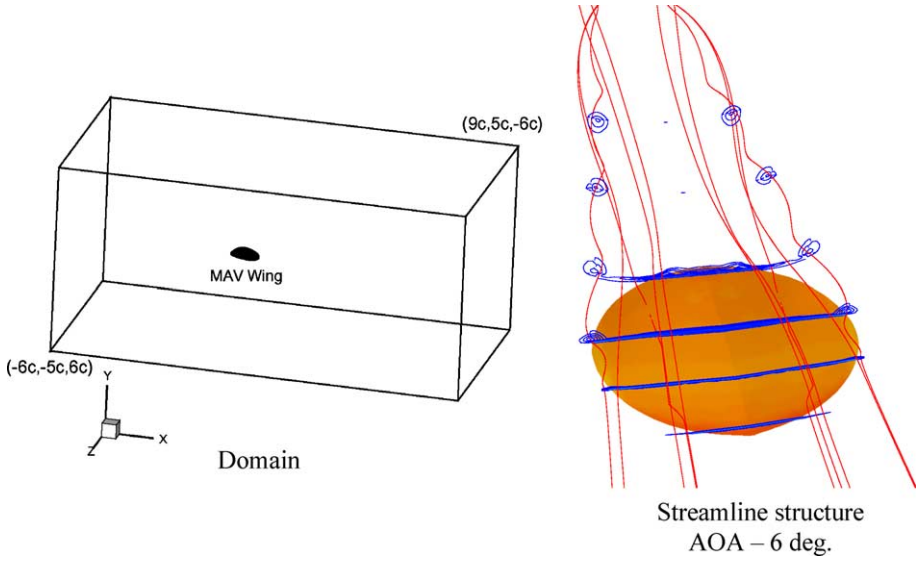

Fig. 6. Computational domain and sample, instantaneous solution of the membrane wing (Lian et al., 2003).

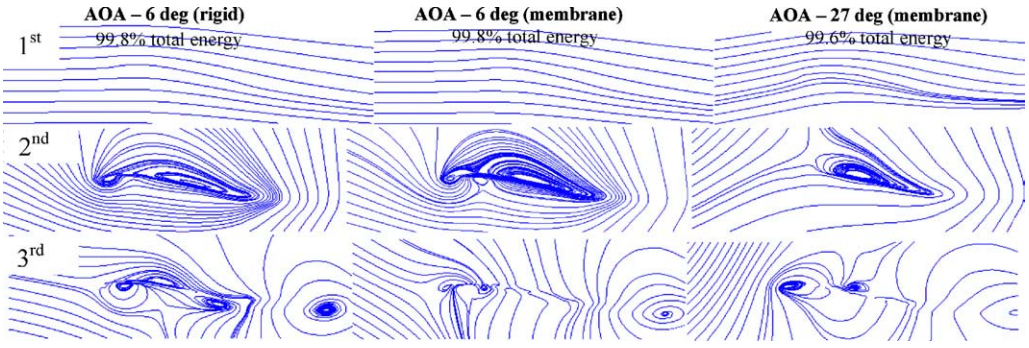

Fig. 7. POD modes showing velocity streamlines for rigid and membrane wing; $\psi_i(r)$; $i = 1,2,3$; $q(r,t) = \vec{V}(r,t)$; extracted at 48.7% span-wise slice.

stresses in our aerodynamic calculations. Unlike the velocity, the pressure responds remarkably to the presence of the moving boundary. The first POD mode of the pressure field ($q(r,t) = p(r,t)$) for the rigid wing case captures 99.9% of the energy, while that of the membrane wing captures just 84.8% energy (for AOA = 6°). This suggests that any parameter that strongly depends on pressure will solicit larger number of POD modes for its adequate representation, in case of a membrane wing. Fig. 8 probes the *mean* convergence of the surface pressure for the membrane wing with error calculations. The L_2 norm of the *time-averaged* surface pressure converges monotonically and dramatically within few POD modes. However, this observation may be elusive to predicting the *instantaneous* pressure convergence, and subsequently the convergence of the *instantaneous* aerodynamic coefficients, which are obtained by an integral analysis on the surface pressure. Fig. 9 demonstrates a non-monotonic convergence for the instantaneous lift-drag ratio for both kinds of wings. However, the excursions from the actual value are highly pronounced for

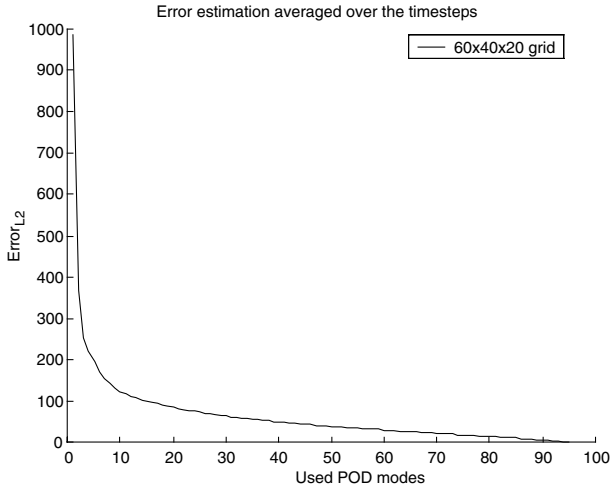

Fig. 8. Time-averaged L_2 error norm of pressure versus numbers of eigenmodes for membrane wing; AOA—6°.

the membrane wing. The rigid wing in comparison requires fewer modes for reasonable accuracy in predict-

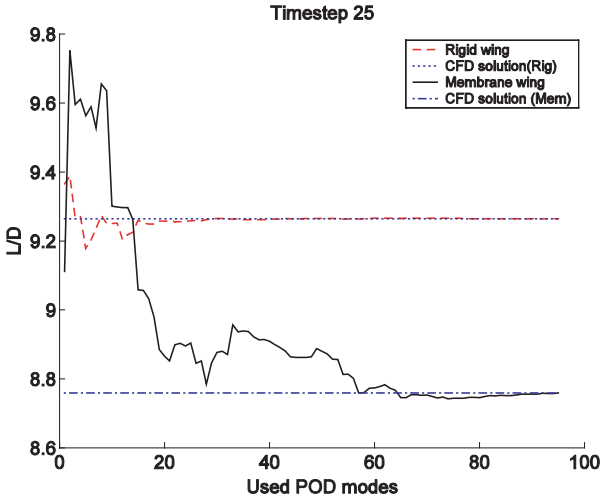

Fig. 9. Instantaneous lift-drag ratio versus numbers of eigenmodes; AOA—6°

ing the aerodynamic performance. This points the fact that moving boundary may coarsen the POD representation of time-dependent aerodynamic coefficients although the overall (mean) dynamic behavior may be appreciably recovered.

4.3. Gallium fusion with laminar natural convection

The schematic of the gallium fusion problem is illustrated in Fig. 10. Recent and accurate computational data on this problem are available (Utturkar et al., 2004). These computations are performed on a 2-D Cartesian grid with a newly developed variant of the PISO algorithm. The solid–liquid interface is implicitly modeled by the single-fluid approach in form of a liquid phase fraction, which is restricted to values between 0 and 1. The velocity field in the solid region is appropriately modeled to assume insignificant values. Furthermore, the Boussinesq approximation is considered valid. The flow field in the fusion problem is truly unsteady without a time-invariant mean component, unlike the previous problems. There is a continuous growth in the flow domain and flow scale as the phase boundary traverses the domain. The ability of POD to accommodate these factors is the focal point in our present study.

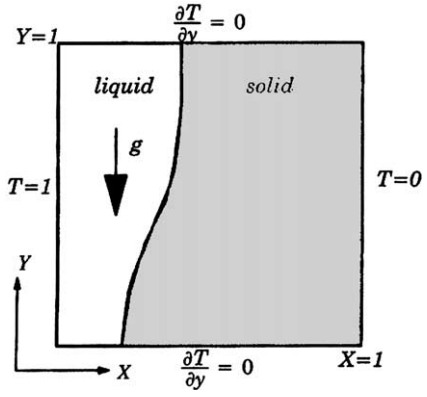

Fig. 10. Schematic of the Gallium fusion problem with the boundary conditions (Utturkar et al., 2004).

Figs. 11 and 12 illustrate the POD eigenmodes and scalar coefficients for the velocity field, for the flow case of $St = 0.042$, $Ra = 2.2 \times 10^3$ and $Pr = 0.0208$. 250 timesteps of the solution, which allow about 75% of the solid to fuse, are employed for the analysis. The energy fractions denote the cumulative kinetic energy recovered by the respective eigenmode. The first POD mode closely resembles the flowfield at the latest time instant. This mode, due to the truly unsteady behavior, is inconsistent with the time-averaged data, as in the previous cases, and just represents the flow structure with highest overall energy content. The following eigenmodes progressively represent the smaller structures in the flowfield. The structures shown by these successive modes are non-physical and are comparable to the harmonics in Fourier series decomposition. The first four modes of the chosen case recover almost 99% of the kinetic energy. However, as explained further, this fact may be misleading to offer a concise representation under certain conditions.

The scalar coefficients (Fig. 12) too show clear trends in their time-dependent behavior. They all initiate from zero and peak gradually in decreasing order of their 'mode number'. Thus, the scalar coefficient of the first mode peaks latest. While the first peak in any coefficient denotes the dominance of the flow scales depicted by the respective eigenmode, the following peaks are relatively insignificant. This is because they are superseded by the coefficients of the preceding eigenmodes. Fig. 13 plots the 'eigenmode number' versus the time instance when

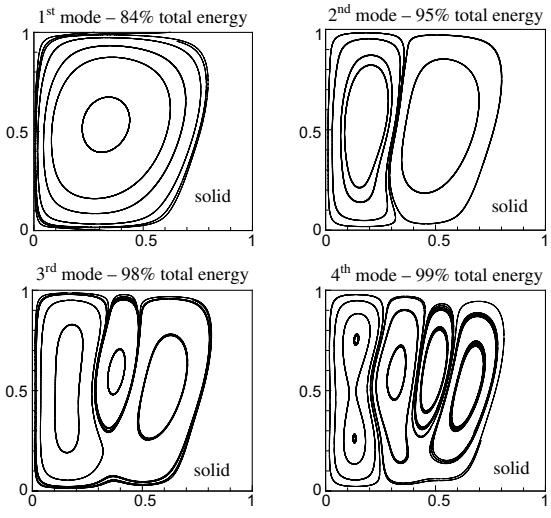

Fig. 11. POD modes showing velocity streamlines ($\psi_i(r)$; $i = 1, 2, 3, 4$) for $St = 0.042$, $Ra = 2.2 \times 10^3$ and $Pr = 0.0208$ case. $q(r, t) = \vec{V}(r, t)$.

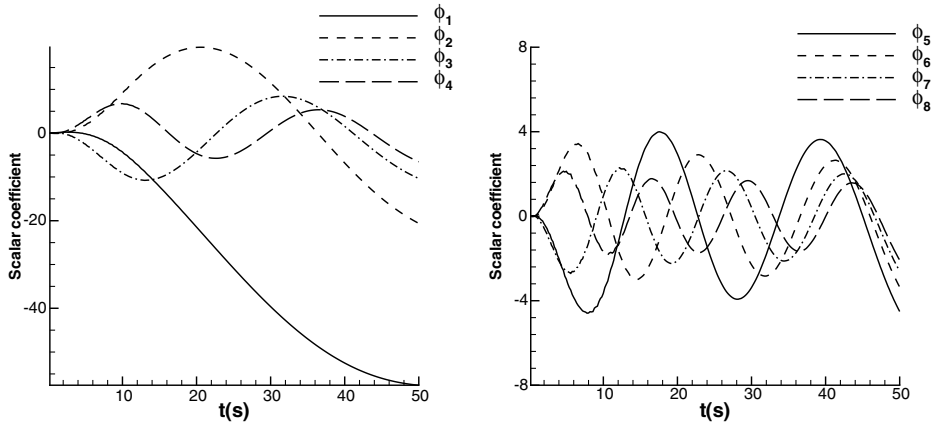

Fig. 12. Scalar coefficients ($\phi_i(t)$; $i = 1, 2, \ldots, 8$) for $St = 0.042$, $Ra = 2.2 \times 10^3$ and $Pr = 0.0208$ case. $q(r,t) = \vec{V}(r,t)$.

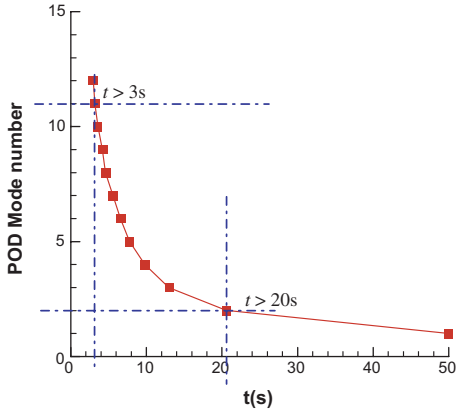

Fig. 13. Time instants when coefficients of respective POD modes show the first peak; $St = 0.042$, $Ra = 2.2 \times 10^3$ and $Pr = 0.0208$ case.

the scalar coefficient shows its first peak. For instance, the second eigenmode peaks at $t = 20$ s, whereas the 12th mode peaks as early as $t = 3$ s. Thus, at least two modes are required to represent the flow scales from any time $t > 20$ s. In comparison, a reduced-order description for the flow from $t > 3$ s solicits at least 12 modes. This argument can be strengthened by observing the centerline vertical velocity profiles at time $t = 3$ s, from Fig. 14. The solid region, as seen from the plots, is manifested as a sharp discontinuity in the velocity field. Although the velocity profile using 10 eigenmodes tends to represent the liquid region reasonably, it produces ripples in the solid region. The ripples are gradually attenuated by incorporating smaller scales of the higher-order POD modes; for instance, 15 modes provide an appreciable representation of the profile at $t = 3$ s for both the phases, as seen from the figure. While the first 12 modes construct the flow scales in the liquid region, the additional modes suppress the oscillations in the solid zone. The above facts are corroborated by the CFD data and the re-constructed data, observed in Figs. 15 and 16, for two widely separated time instants. Impact of POD on the thermal field is not discussed here, because it is expected to be of similar nature. In general, the efficacy of a POD representation may strongly depend on the time interval of interest for truly unsteady problems, and may not merely rely on the energy content.

5. Summary and conclusion

The POD approach is a valuable tool for fluid dynamics confined in fixed geometries. For fluid flows with moving boundaries, the boundary location, shape, and movement cannot be prescribed a priori, and need

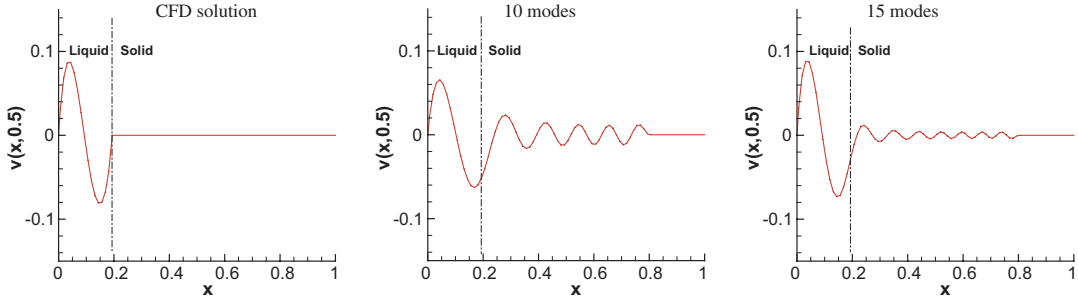

Fig. 14. Horizontal-centerline vertical velocities for $St = 0.042$, $Ra = 2.2 \times 10^3$ and $Pr = 0.0208$ case at $t = 3$ s.

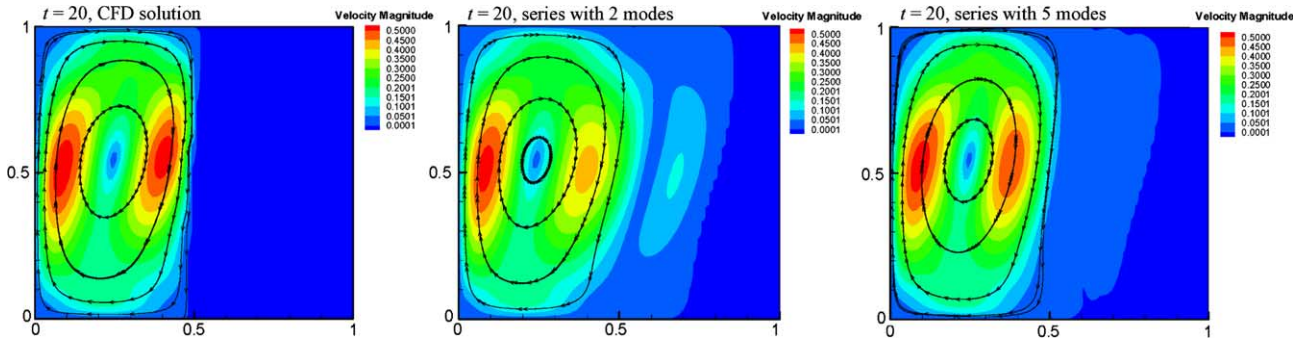

Fig. 15. Comparison between CFD solution and re-constructed solution for $St = 0.042$, $Ra = 2.2 \times 10^3$ and $Pr = 0.0208$ case at $t = 20$ s. Contours represent velocity magnitude and lines represent streamlines.

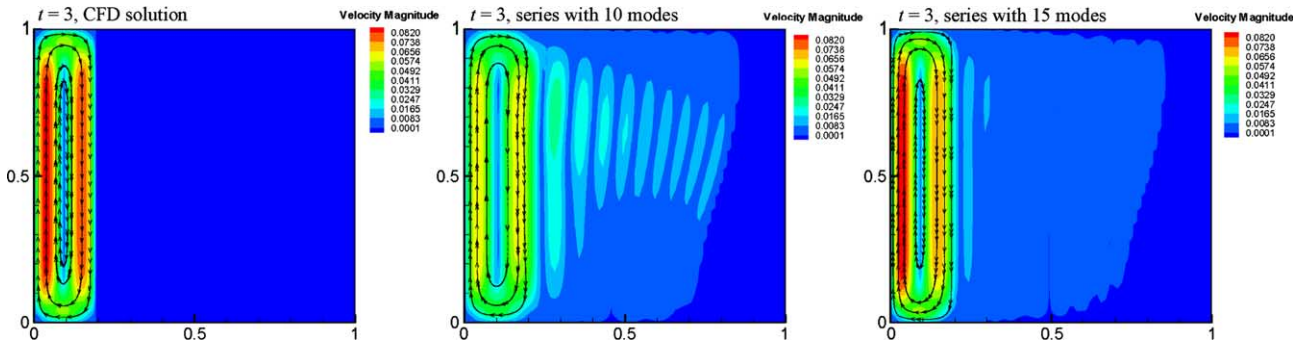

Fig. 16. Comparison between CFD solution and re-constructed solution for $St = 0.042$, $Ra = 2.2 \times 10^3$ and $Pr = 0.0208$ case at $t = 3$ s. Contours represent velocity magnitude and lines represent streamlines.

to be tracked as a part of the solution. In the computational process, the boundary information and the field equations are solved in synchronization, and thus the effectiveness of the POD approach for complex fluid flow problems with moving boundaries needs to be assessed. The well-established technique of POD is examined for fluid flow with moving boundaries, in the context of cavitating and phase change flows, and fluid–membrane interaction. The unsteady simulation data are analyzed to observe the adequacy in the POD representation. The present study has demonstrated that POD can offer valuable insight by extracting the salient features from the solution obtained.

The cavitating flow simulations are investigated by the reduced-order approach to distill the effect of turbulence modeling. The flow structure and time-dependent behavior of the Launder–Spalding model is compared to that of the newly developed filter-based model. Phase plane plots are utilized to depict various POD modes through a dynamic framework. The lower-order eigenmodes of the flow field, for both turbulence models, at the higher cavitation number, show consistency in the flow structure. The significant difference observed in the lift-drag behavior for the two models is mainly manifested into the time-dependent scalar coefficients. Conversely, at the lower cavitation number, where the void forming intensity is higher, the turbulence-closure registers a second-order impact on the flow structure. This is mainly because of the multi-timescales produced by the filter-based turbulence model, which diffuse into the higher-order eigenmodes and alter the flow pattern. The Launder–Spalding model demonstrates a rapid dissipation of cavitation instabilities at all significant energy levels. In comparison, the filter-based model is able to sustain even the higher-order unsteady tendencies in the flow. The lack of experimental data on the hydrofoil case restricts quantitative appraisal of the latest turbulence model. However, the present effort certainly endorses its intended behavior; at least, within the scope of cavitating flows.

POD computations for 3-D, membrane wing flow are presented for two different angles-of-attack. The results, in turn, are contrasted to a case with a rigid wing. The issue of moving grid is handled by interpolating the solution, at every time step, on to a fixed grid before performing POD. The eigenmodes of the velocity field progressively discern the influence of the flexible membrane and AOA on the flow. Despite the fact, the velocity field shows rapid convergence for all the cases. Conversely, the convergence of the pressure field is impeded because of the moving boundary interactions. Though the energy content and the *time-averaged* data depict a monotonous convergence within few POD modes, the *instantaneous* values of aerodynamic coefficients,

obtained from the reduced-order data, require larger number of modes to agree with the actual data. Thus, if primary interests lie in the accurate representation of the velocity field, very few POD modes may be sufficient for assessment. However, reduced-order analysis of the aerodynamic performance, which is strongly dictated by the pressure, may be coarsened by moving membrane dynamics.

The case of gallium fusion with natural convection is considered for a POD investigation because of its phase front propagation. The POD eigenmodes successively extract the smaller scales in the flow structure. While few modes can sufficiently construct a reduced-order representation for the later time interval of the flow, a larger number of modes are required to provide the flow scales for the initial part of the fusion process. As a caveat, in case of inherently time-dependent flows, effective POD representation may be sensitive to the time interval of interest, and merits a further inspection beyond the energy convergence of the eigenmodes.

Acknowledgment

The present research has been supported in part by NASA and US Air Force.

References

Ahlman, D., Soderlund, F., Jackson, J., Kurdilla, A., Shyy, W., 2002. Proper orthogonal decomposition for time-dependent lid-driven cavity flows. Numer. Heat Transfer, Part B 42, 285–306.

Annaswamy, A., Choi, J.J., Sahoo, D., Alvi, F.S., Lou, H., 2002. Active closed loop control of supersonic impinging jet flows using POD models. In: Proceedings of 41st IEEE Conference on Decision and Control, pp. 3294–3299.

Arian, E., Fahl, M., Sachs, E.W., 2002. Managing POD models by optimization methods. In: Proceedings of 41st IEEE Conference on Decision and Control, pp. 3300–3305.

Aubry, N., Holmes, P., Lumley, J.L., Stone, E., 1988. The dynamics of coherent structures in the wall region of the wall boundary layer. J. Fluid Mech. 192 (15).

Bera, J.C., Michard, M., Grosjean, N., Comte-Bellot, G., 2001. Flow analysis of two-dimensional pulsed jets by particle image velocimetry. Exp. Fluids 31, 519–532.

Cizmas, P.G.A., Palacios, A., 2003. Proper orthogonal decomposition of turbine rotor–stator interaction. J. Propulsion Power 19 (2), 268–281.

Colonius, T., Rowley, C.W., Freund, J.B., Murray, R., 2002. On the choice of norm for modeling compressible flow dynamics at reduced-order using the POD. In: Proceedings of 41st IEEE Conference on Decision and Control, pp. 3273–3278.

Delville, J., Ukeiley, L., Cordier, L., Bonnet, J.P., Glauser, M., 1999. Examination of large-scale structures in a turbulent plane mixing layer: Part 1—proper orthogonal decomposition. J. Fluid Mech. 391, 91–122.

Gunther, A., Rohr, P.R., 2002. Structure of temperature field in a flow over heated waves. Exp. Fluids 33, 920–930.

Johansen, S., Wu, J., Shyy, W., 2004. Filter-based unsteady RANS computations. Int. J. Heat Fluid Flow 25 (1), 10–21.

Kostas, J., Soria, J., Chong, M.S., 2002. Particle image velocimetry measurements of a backward-facing step flow. Exp. Fluids 33, 838–853.

Launder, B.E., Spalding, D.B., 1974. The numerical computation of turbulent flows. Comp. Meth. Appl. Mech. Eng. 3, 269–289.

Lian, Y., Shyy, W., Viieru, D., Zhang, B., 2003. Membrane wing aerodynamics for micro aerial vehicles. Prog. Aerospace Sci. 39, 425–465.

Liberzon, A., Gurka, R., Hetsroni, G., 2001. Vorticity characterization in a turbulent boundary layer using PIV and POD analysis. In: 4th International Symposium on Particle Image Velocimetry, Gottingen, Germany, Paper 1184.

Lucia, D.J., King, P.I., Beran, P.S., 2002. Domain decomposition for reduced-order modeling of a flow with moving shocks. AIAA J., Tech. Notes 40 (11), 2360–2362.

Lumley, J.L., 1967. The structure of inhomogeneous turbulent flows. Atmos. Turbu. Radio Wave Propagat., 166–178.

Lumley, J.L., Poje, A., 1997. Low dimensional models for flows with variable density. Phys. Fluids 9 (7), 2023–2031.

Picard, C., Delville, J., 2000. Pressure–velocity coupling in a subsonic round jet. Int. J. Heat Fluid Flow 21, 359–364.

Podvin, B., 2001. On the adequacy of the ten-dimensional model for the wall layer. Phys. Fluids 13 (1), 210–224.

Prabhu, R.D., Collis, S.S., Chang, Y., 2001. The influence of control on proper orthogonal decomposition of wall-bounded turbulent flow. Phys. Fluids 13 (2), 520–537.

Press, W.H., Teukolsky, S.A., Vetterling, W.T., Flannery, B.P., 1992. Numerical Recipes in Fortran—The Art in Scientific Computing. Cambridge University Press, New York.

Senocak, I., Shyy, W., 2002. A pressure-based method for turbulent cavitating flow computations. J. Comp. Phys. 176, 363–383.

Senocak, I., Shyy, W., 2004a. Interfacial dynamics-based modeling of turbulent cavitating flows, Part-1: Model development and steady-state computations. Int. J. Numer. Meth. Fluids 44, 975–995.

Senocak, I., Shyy, W., 2004b. Interfacial dynamics-based modeling of turbulent cavitating flows, Part-2: Time-dependent computations. Int. J. Numer. Meth. Fluids 44, 997–1016.

Sirovich, L., 1987. Turbulence and the dynamics of coherent structures: Part I–III. Quart. Appl. Math. 45, 561–590.

Thakur, S.S., Wright, J., Shyy, W., 2002. STREAM: A computational fluid dynamics and heat transfer Navier–Stokes solver. Streamline Numerics Inc. and Computational Thermo-Fluids Laboratory, Department of Mechanical and Aerospace Engineering Technical Report, Gainesville, Florida.

Ukeiley, L., Cordier, L., Manceau, R., Delville, J., Glauser, M., Bonnet, J.P., 2001. Examination of large-scale structures in a turbulent plane mixing layer: Part 2—Dynamical systems model. J. Fluid Mech. 441, 67–108.

Ukeiley, L., Kannepalli, C., Arunajatesan, S., 2002. Development of low dimensional models for control of compressible flows. In: Proceedings of 41st IEEE Conference on Decision and Control, pp. 3282–3287.

Utturkar, Y., Thakur, S., Shyy, W., 2004. Accurate time-dependent computations and reduced-order modeling for multiphase flow. ASME Paper HT-FED2004-56236.

Wu, J., Utturkar, Y., Senocak, I., Shyy, W., Arakere, N., 2003a. Impact of turbulence and compressibility modeling on three-dimensional cavitating flow computations. AIAA Paper 2003–4264.

Wu, J., Utturkar, Y., Shyy, W., 2003b. Assessment of modeling strategies for cavitating flow around a hydrofoil. In: Fifth International Symposium on Cavitation, Osaka, Japan (Online Library—http://flow.me.es.osaka-u.ac.jp/cav2003/).

Zhang, B., Lian, Y., Shyy, W., 2003. Proper orthogonal decomposition for three-dimensional membrane wing aerodynamics. AIAA Paper 2003–3917.